X- AND γ-RAY PULSATIONS OF THE NEARBY RADIO-FAINT PSR J1741−2054

M. MARELLI[1], A. BELFIORE[1,2], P. SAZ PARKINSON[2,3], P. CARAVEO[1,4], A. DE LUCA[1,4], C. SARAZIN[5],
D. SALVETTI[1,4,6], G. R. SIVAKOFF[5,7], AND F. CAMILO[8,9]

[1] INAF–Istituto di Astrofisica Spaziale e Fisica Cosmica Milano, via E. Bassini 15, I-20133 Milano, Italy; marelli@lambrate.inaf.it
[2] Santa Cruz Institute for Particle Physics, University of California, Santa Cruz, CA 95064, USA
[3] Department of Physics, The University of Hong Kong, Pokfulam Road, Hong Kong
[4] Istituto Nazionale di Fisica Nucleare, Sezione di Pavia, Via Bassi 6, I-27100 Pavia, Italy
[5] Department of Astronomy, University of Virginia, P.O. Box 400325, Charlottesville, VA 22904-4325, USA
[6] Università degli Studi di Pavia, Strada Nuova 65, I-27100 Pavia, Italy
[7] Department of Physics, University of Alberta, CCIS 4-183 Edmonton, AB T6G 2E1, Canada
[8] Columbia Astrophysics Laboratory, Columbia University, New York, NY 10027, USA
[9] Arecibo Observatory, HC3 Box 53995, Arecibo, PR 00612, USA

ABSTRACT

We report the results of a deep *XMM-Newton* observation of the radio-faint γ-ray pulsar J1741−2054 and its nebula together with the analysis of five years of *Fermi* Large Area Telescope (LAT) data. The X-ray spectrum of the pulsar is consistent with an absorbed power law plus a blackbody, originating at least partly from the neutron star cooling. The nebular emission is consistent with that of a synchrotron pulsar wind nebula, with hints of spatial spectral variation. We extended the available *Fermi* LAT ephemeris and folded the γ-ray and X-ray data. We detected X-ray pulsations from the neutron star: both the thermal and non-thermal components are ∼35%–40% pulsed, with phase-aligned maxima. A sinusoid fits the thermal-folded profile well. A 10 bin phase-resolved analysis of the X-ray emission shows softening of the non-thermal spectrum during the on-pulse phases. The radio, X-ray, and γ-ray light curves are single-peaked, not phase-aligned, with the X-ray peak trailing the γ-ray peak by more than half a rotation. Spectral considerations suggest that the most probable pulsar distance is in the 0.3–1.0 kpc range, in agreement with the radio dispersion measure.

Key words: gamma rays: stars – pulsars: general – pulsars: individual (PSR J1741-2054) – stars: neutron – X-rays: stars

Online-only material: color figure

1. INTRODUCTION

The launch of the *Fermi γ-ray Space Telescope* offered the first opportunity to study a sizeable population of γ-ray pulsars. The *Fermi* Large Area Telescope (LAT; Atwood et al. 2009) has discovered pulsed γ-ray signals from more than 150 objects (Abdo et al. 2013), revolutionizing our view of them and giving birth to new high-energy pulsar sub-families, such as millisecond (see, e.g., Abdo et al. 2009b; Ransom et al. 2011; Keith et al. 2011; Espinoza et al. 2013) and radio-quiet γ-ray pulsars (see, e.g., Abdo et al. 2009a; Saz Parkinson et al. 2010; Pletsch et al. 2013), as numerous as the classic family of young, radio-loud pulsars (Caraveo 2013). The wealth of detections confirms the importance of the γ-ray channel in the overall energy budget of rotation-powered pulsars and paves the way to understanding the three-dimensional structure and electrodynamics of neutron star magnetospheres. Indeed, radio and γ-ray light curves contain a great deal of useful information about pulsar emission processes (see, e.g., Watters & Romani 2011; Pierbattista et al. 2012, 2014), confirming that models with emission originating at high altitudes in the magnetosphere (e.g., outer and slot-gap; Cheng et al. 1986; Harding & Muslimov 2004) are favored over models with near-surface emission (e.g., polar cap; Harding 2013).

Fitting γ-ray and radio light curves simultaneously is a promising way to constrain pulsar geometric parameters (e.g., Pierbattista et al. 2014). Using the information in the (magnetospheric) non-thermal pulsar X-ray light curves could further improve the approach, adding another piece to the pulsar emission puzzle. This approach could localize the emitting region(s) responsible for the non-thermal pulsed X-ray emission with respect to the high altitude gamma-ray emitting region.

Few X-ray light curves have been exploited for modeling magnetospheric emission, compared to γ-ray profiles. This is largely due to the lack of high-quality X-ray light curves, primarily due to the occasional and non-targeted observational efforts. At this time, ∼60 out of 77 young pulsars in the second *Fermi* LAT pulsar catalog (2PC; Abdo et al. 2013) have been detected in X-rays (Becker 2009; Marelli et al. 2011; Marelli 2012; Abdo et al. 2013), but X-ray pulsations have been detected from fewer than half of them. Only nine *Fermi* pulsars have both the high X-ray fluxes and the long dedicated X-ray observations needed to disentangle the thermal and the non-thermal pulsations. Only five of these (Crab, Vela, Geminga, PSR J0659+1414, and PSR J1057−5226) have been characterized by a multi-bin phase-resolved X-ray spectral analysis (De Luca et al. 2005; Manzali et al. 2007; Weisskopf et al. 2011). Of these, only the Crab (and possibly Geminga, Jackson & Halpern 2005) yielded a non-thermal light curve with a photon index varying with phase, a behavior that is still puzzling (Harding et al. 2008; Tang et al. 2008; Hirotani 2008).

With the notable exception of the Crab among young pulsars, the multiwavelength behavior of isolated neutron stars is complex, with radio, optical, X-ray, and γ-ray light curves usually unaligned, pointing to different emitting regions in the pulsar magnetosphere. The rich phenomenology, in particular including the X-ray information, has not yet been fully exploited for modeling the radiation processes of pulsars, leaving a number of questions unsolved.

Here we report the results of a deep *XMM-Newton* observation intended for phase-resolved X-ray spectral analysis of the *Fermi*

pulsar J1741−2054 (hereafter J1741). The middle-aged J1741 ($\tau_c = 390$ kyr) was discovered in a blind pulsation search of a *Fermi* LAT point source (Abdo et al. 2009a). For a moment of inertia $I = 10^{45}$ g cm^2, its period $P = 413$ ms and period derivative $\dot{P} = 1.7 \times 10^{-14}$ s s^{-1} give a spin-down energy loss rate $\dot{E} = 9\times10^{33}$ erg s^{-1}, clearly on the low side of the γ-ray pulsar distribution (see Figure 1 in Abdo et al. 2013). The pulsar was then detected in archival Parkes radio observations, showing a remarkably low dispersion measure, DM = 4.7 pc cm^{-3} (Camilo et al. 2009). The Galactic electron density model of Cordes & Lazio (2002) yields a distance of ∼0.38 kpc, making J1741 one of the closest γ-ray pulsars known. At this distance, the low observed 1400 MHz radio flux density, $S_{1.4} \sim 160\,\mu$Jy, makes it the faintest radio pulsar known.

At the position obtained from LAT timing analysis (Ray et al. 2011), Abdo et al. (2009a), Romani et al. (2010), and Marelli et al. (2011) found the X-ray counterpart using both *Swift* and *Chandra* data. The *Chandra* observation also revealed diffuse, faint X-ray emission due to a pulsar wind nebula (PWN) trail extending some 2′ at position angle P.A. = 45° ± 5° (north through east). This extended structure was also associated with a 20″ long Hα bow shock. Accurate bow shock modeling by Romani et al. (2010) suggests a pulsar velocity $v_p \sim 150$ km s^{-1} directed 15° ± 10° out of the plane of the sky.

2. X-RAY OBSERVATIONS

Our deep *XMM-Newton* observation of J1741 started on 2013 February 28 at 19:50:39 UT and lasted 70.9 ks. The PN (Struder et al. 2001) of the European Photon Imaging Camera (EPIC) was operating in Small Window mode (time resolution of 5.6 ms over a 4′ × 4′ field of view, FOV), while the Metal Oxide Semiconductor (MOS) detectors (Turner et al. 2001) were set in Full Frame mode (2.6 s time resolution and a 15′ radius FOV). The thin optical filters were used for the PN and MOS cameras. For our analysis, we used the *XMM-Newton* Science Analysis Software (SAS) v13.0. To fully characterize both the pulsar and the nebula, we also used the available *Chandra* Advanced CCD Imaging Spectrometer (ACIS; Garmire et al. 2003) observation of the field, performed on 2010 May 21 and lasting 48.8 ks (these data were included in Romani et al. 2010). To better characterize the pulsar, we also took advantage of the ∼300 ks of data collected as part of the Cycle 14 *Chandra* Visionary Project "A Legacy Study of the Relativistic Shocks of PWNe" by R. Romani. We retrieved "level 1" data from the *Chandra* Science Archive and used the *Chandra* Interactive Analysis of Observation (CIAO) software v.4.3. For all the data sets, we followed the standard data processing approach, using the same procedures reported in Marelli et al. (2013).

3. γ-RAY ANALYSIS

The *Fermi* LAT data set we used to extend the γ-ray ephemeris of J1741 spans five years, from 2008 August 4 to 2013 August 4. P7REP Source class events were selected with reconstructed energies from 0.1 to 100 GeV from an area within 20° of the source position. We excluded γ-rays collected when the LAT was not in nominal science operations mode, when the spacecraft rocking angle exceeded 52°, when the Sun was within 5° of the pulsar position, and those with measured zenith angles >100°, to reduce contamination by residual γ-rays from the bright limb of the Earth. We performed a binned maximum likelihood analysis, as reported in Abdo et al. (2013). We used the

Fermi Science tools v09r32p04, instrument response functions P7REP_SOURCE_V15, and the Galactic and isotropic models obtained by the LAT collaboration from the analysis of four years of data. The analysis tools, instrument response functions, and diffuse emission models are available from the *Fermi* Science Support Center, http://fermi.gsfc.nasa.gov/ssc. The source models were taken from the two-year catalog (Nolan et al. 2012) and 2PC. Post-fit spatial residuals did not reveal the need for any additional sources, beyond those in the two-year catalog, in our model of the region. The pulsar γ-ray spectrum is consistent with a power law with an exponential cutoff with a photon index $\Gamma = 1.10 \pm 0.10$ and cutoff energy $E_c = 0.92 \pm 0.06$ GeV. These results are in full agreement with those in 2PC.

The *Fermi* Science Tool gtsrcprob combines the spectral results with the LAT's energy-dependent point-spread function (PSF) to assign each event its probability of coming from the pulsar (Kerr 2011). We used only barycentered events with a probability higher than 0.01 for the following timing analysis. The rotation ephemeris used in 2PC spans only 3 yr: we extended it, using a weighted Markov Chain Monte Carlo algorithm (MCMC; see, e.g., Wang et al. 2013). Adding six months of data in each iteration, we re-evaluated the timing solution using the weighted H test (see, e.g., De Jager & Busching 2010). The highest H value of 4782.59 (20 harmonics) for five years of data was found for $F_0 = 2.41720384698$ Hz, $F_1 = -9.93133$e-14, $F_2 = -5.924$e-25, and $F_3 = 5.75$e-32, with epoch zero at MJD 55631.0002.[10]

With this ephemeris, we assigned a rotational phase to each γ-ray event and filled a 100 bin >0.1 GeV phase histogram with bin uncertainties using the photon weights, following Abdo et al. (2013; see Section 6).

We performed a γ-ray phase-resolved spectral analysis on the five-year data set. For 20 phase bins, we re-ran the binned spectral analysis, leaving only one or more of the pulsar parameters (normalization, photon index, and energy cutoff) free to vary. The Test Statistic value (see, e.g., Mattox at al. 1996) does not vary significantly by freeing one or two of the parameters so that the addition of the additional degrees of freedom are not justified. Moreover, with both the photon index and the cutoff energy free, their fit with a constant is acceptable (null hypothesis probability nhp = 6×10^{-4} and 6×10^{-3} for the photon index and cutoff, respectively). Thus, we found no indication of spectral variation as a function of the pulsar phase.

4. X-RAY IMAGING AND SOURCE DETECTION

Following the method reported in Marelli et al. (2013), we detected and selected the active galactic nucleus (AGN) like serendipitous sources in the *XMM-Newton* and *Chandra* FOVs (see Figure 1). The spectra of these sources were fitted together, linking their hydrogen column densities N_H to assess the average Galactic absorption column. The resulting value, $N_H^{gal} = (4.54 \pm 0.36) \times 10^{21}$ cm^{-2} (90% confidence error), is slightly greater than the value of 3×10^{21} cm^{-2} obtained from the 21 cm H I sky survey of Kalberla et al. (2005). This points to the absence of thick molecular clouds in the *XMM-Newton* FOV. Since N_H^{gal} obtained from X-ray absorption probes all types of nuclei along the line of sight, whereas the latter value samples only atomic hydrogen, this observed value of N_H is to be expected (Dickey & Lockman 1990).

---

[10] The rotation ephemeris is available at http://fermi.gsfc.nasa.gov/ssc/data/access/lat/ephems/.
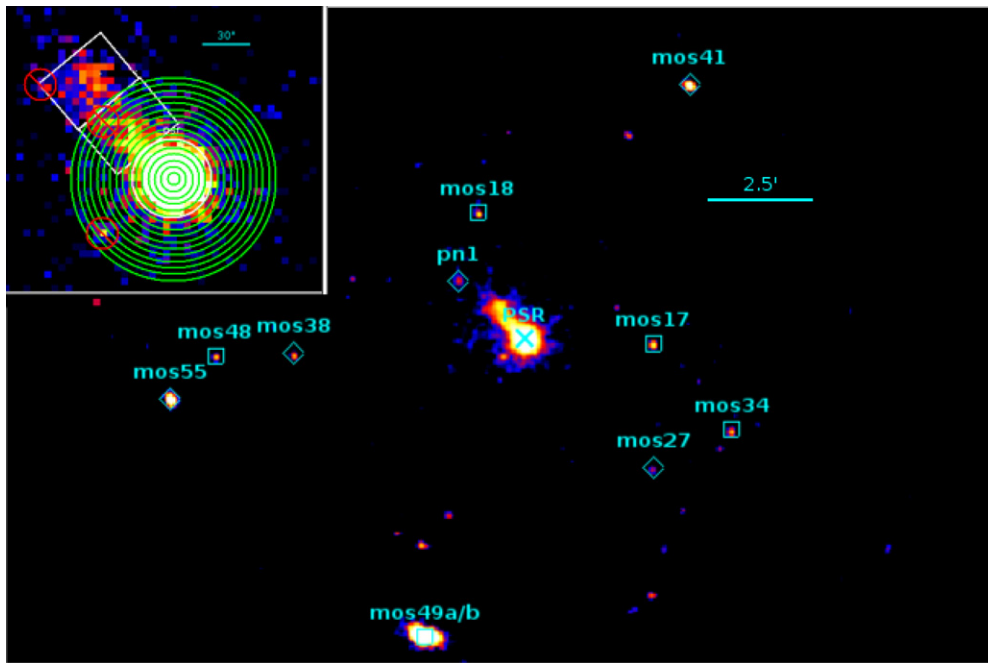
Figure 1. Combined exposure-corrected 0.3–6 keV FOV images of the three *XMM-Newton* cameras. We applied a Gaussian filter with a kernel radius of $3''$. Cyan symbols mark the sources, detected with $>6\sigma$ confidence level and with more than 225 detected counts, that we analyzed to constrain the value of the Galactic absorption column. The squares mark the AGN-like sources, diamonds mark other field sources, and the cross marks the pulsar. (Upper left) Expanded image of the pulsar and its tail. Green annuli mark the regions we used for the PSF analysis (with the exception of the nebular region); we extracted photons to build the pulsar and nebular spectra from white regions; red regions mark the point-like sources we excluded from analysis.

Apart from the pulsar itself, the main feature apparent in the PN FOV is the PWN emission. To find the best extraction regions for the pulsar and the nebula, as well as to better evaluate the PWN shape, we created exposure-corrected radial (around the pulsar) and linear (parallel and orthogonal to the main axis of the nebula) brightness profiles in the 0.3–10 keV energy range. The radial profile is consistent (nhp = 0.14) with the nominal instrument PSF[11] only up to $40''$ from the pulsar due to the relative faintness of the nebula. The linear profile, with $1'$ width centered on the pulsar and orthogonal to the main axis of the nebula, is also consistent (nhp = 0.009) with the PSF, proving the absence of a detectable nebular component in the orthogonal region. The presence of the nebula in the profile parallel to the main axis is apparent, extending up to $\sim2'$ from the pulsar and with flux decreasing with distance (apparent in Figure 1, see also Romani et al. 2010). From the deep *Chandra* observations, the unusual shattered shape of the tail-like nebula is apparent, appearing to be divided into three blobs.

5. PHASE-INTEGRATED SPECTRAL ANALYSIS

Using a $25''$ radius extraction circle around the pulsar, we obtained 9794, 2983, and 3073 counts in the 0.3–10 keV energy range in the PN and the two MOS detectors, respectively, with a background contribution of less than 4%. We also used 19,380 pulsar counts from the *Chandra* observations. For the spectral analysis, we followed Marelli et al. (2013). To better constrain the column density, we fitted the nebular spectra together with the pulsar spectrum. We obtained 1508, 557, and 533 counts in the 0.3–10 keV energy range in the PN and the two MOS detectors, respectively, with a background contribution of

40% and 25%. We obtained 5633 nebular counts, with a 30% background contribution from the *Chandra* observations.

One-component models are not statistically acceptable for the pulsar spectrum ($\chi_r^2 = 2.2$, nhp ~ 0 for an absorbed power law and $\chi_r^2 = 11.6$, nhp = 0 for an absorbed blackbody, where the χ^2 has been reduced for 781 degrees of freedom, or "dof"). The pulsar spectrum is consistent ($\chi_r^2 = 1.18$, nhp = 2×10^{-3}, 779 dof) with a combination of a power-law component with a photon index of $\Gamma = 2.68 \pm 0.04$ (90% confidence errors) and a blackbody with a temperature of $T = (7.07 \pm 0.19) \times 10^5$ K, and an emitting radius $R = (5.39^{+0.81}_{-0.71}) \times d_{380}$ km (where d_{380} is the distance of the pulsar in units of 380 pc, derived from the dispersion measure of the pulsar using the NE2001 electron model of the Galaxy; Camilo et al. 2009), absorbed by a column density of $N_H = (1.21 \pm 0.01) \times 10^{21}$ cm^{-2}, about one-fourth of the Galactic value. The PWN spectrum is consistent with an absorbed power law with $\Gamma = 1.74 \pm 0.07$. The unabsorbed fluxes of the non-thermal and thermal components of the pulsar spectrum are $5.47 \pm 0.13 \times 10^{-13}$ and $7.63 \pm 0.19 \times 10^{-13}$ erg cm^{-2} s^{-1}, respectively. The unabsorbed nebular flux is $1.40 \pm 0.09 \times 10^{-13}$ erg cm^{-2} s^{-1}. We note that a three-component model is not statistically compelling (for a power law plus double blackbody, we obtain $\chi_r^2 = 1.18$, nhp = 3×10^{-3}, 777 dof). We also note that a composite non-thermal plus a magnetized neutron star atmosphere model (nsa in XSpec; assuming a neutron star with a radius of 12 km, mass of 1.4 $M_\odot$, and a surface magnetic field of 10^{13} G) gives a very poor fit. We obtain a $\chi_r^2 = 1.22$, nhp = 7×10^{-5}, 779 dof, with a lower emitting temperature of $(3.02 \pm 0.12) \times 10^5$ K.

To study the possible spectral variation of the nebula with angular distance from the pulsar, we divided the nebula into three different regions on the basis of their angular separations from the pulsar. We chose to equally divide the main axis of the ellipsoidal nebular region in order to consider the three
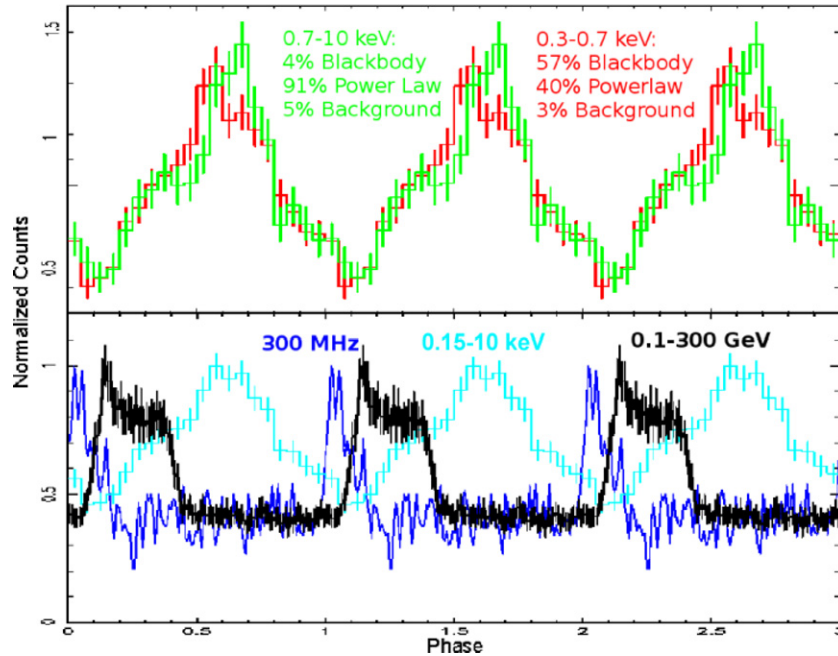

Figure 2. Top: EPIC/pn folded light curves in different energy ranges. X-ray photon phases were computed according to the *Fermi* LAT ephemeris overlapping with the *XMM-Newton* data set, with selection as in Section 6. The red curve contains photons in the 0.3–0.7 keV energy range and the green one in the 0.7–10 keV range. The curves have been renormalized by dividing each bin by N_{counts}/N_{bins}, where N_{counts} is the total number of events in the energy range and N_{bins} the number of bins (1σ errors are shown). Bottom: phased radio, X-ray, and γ-ray light curves of PSR J1741−2054. The 300 MHz radio light curve, shown in blue, comes from the Green Bank Observatory (Camilo et al. 2009). The 100 bin γ-ray curve, shown in black, contains all the five-year *Fermi* LAT weighted counts with energies >100 MeV. The 20 bin X-ray curve is shown in cyan. All the curves have been renormalized to have the highest bin value equal to 1 (1σ errors are shown).

(A color version of this figure is available in the online journal.)

blobs. The different PSFs, as well as different exposure maps, of the two X-ray instruments have been taken into account. All the parameters of the spectra from the corresponding regions in *Chandra* and *XMM-Newton* observations were linked, also freezing the absorption column to the previously fitted value. We see marginal evidence for a spectral variation (in fact, linking the photon index for the three spectra, we obtain $\chi^2_r = 1.45$, nhp = 6.4×10^{-5}, 184 dof), with $\Gamma_{near} = 1.72 \pm 0.09$ (90% confidence errors), $\Gamma_{med} = 1.90 m \pm 0.10$, and $\Gamma_{far} = 1.69 \pm 0.09$.

6. PULSAR TIMING ANALYSIS

For the timing analysis, a PATTERN selection was performed as by Marelli et al. (2013) and the X-ray photon arrival times were barycentered to the *Chandra* source position (R.A., decl. (J2000) 17:41:57.28, −20:54:11.8) from Romani et al. (2010), which is consistent with the γ-ray timing position. We then phase-folded the X-ray photons using our *Fermi* LAT timing solution, contemporaneous with our *XMM-Newton* data set. We extracted 11,507 PN events in the 0.15–10 keV energy range from the 25″ circle centered on the pulsar. We repeated the exercise for photons in different energy ranges.

Pulsations with >20σ significance appear in the 0.15–10 keV energy range (H-test = 585; tail probability = 0, and $\chi^2_r = 29$, 19 dof, according to a χ^2 test on the folded curve testing a constant model). The profile has a single peak, lagging the radio peak by 0.6 in phase. Light curves for different energy ranges are shown in Figure 2, phase-aligned with the γ-ray and radio profiles. Using the phase-averaged composite spectrum, we evaluated the background contribution, the pulsar blackbody, and the power-law components in different energy ranges, as in Caraveo et al. (2010). We obtained a background-subtracted pulsed fraction of 36.1% ± 1.5% in the 0.3–10 keV energy range. Dividing the energy range into low energy (0.3–0.7 keV,

where the blackbody accounts for ∼60% of the counts) and high-energy bands (0.7–10 keV, where the power law accounts for ∼90% of the counts) we obtained pulsed fractions of 35.8% ± 1.5% and 36.4% ± 1.5%, respectively. We know the pulsed fraction in each band and the percentage of blackbody, power-law, and background contributions so that we can get the net pulsed fraction of the two spectral components. The pulsar's power law is pulsed at ∼38% and the blackbody component at ∼36%. Although at lower energies, the curve is quasi-sinusoidal (a fit with a sinusoid gives $\chi^2_r = 1.31$, 17 dof, nhp = 0.17) due to the blackbody contribution, the profile at higher energies is not compatible with a sinusoid ($\chi^2_r = 2.70$, 17 dof, nhp = 10^{-4}). The correlation of the power-law photon index with its normalization (see, e.g., Figure 4) somewhat biases the normalization profile in Figure 3, while the counts profiles in Figure 2 are better suited for comparing their shapes. The peak positions at low (0.3–0.7 keV) and high (0.7–10 keV) X-ray energies are separated by less than 0.1 in phase, but they are offset by about a half-rotation from the main γ-ray pulse and the radio pulse (following Abdo et al. (2013), the radio pulse leads the γ-ray pulse by 0.074 ± 0.006 in phase).

7. PHASE-RESOLVED PULSAR ANALYSIS

To search for possible variation of the X-ray spectral parameters with rotational phase, we first fitted the on- and off-pulse spectra. We define the on-pulse interval to be between phase 0.3 and 0.8 (values obtained from a fit with a double-step model) and the remaining phase bins as off-pulse. Fitting only the power-law counts ($E > 0.7$ keV), we fixed the column density and the photon index to the phase-averaged values, obtaining an acceptable nhp = 0.047 ($\chi^2_r = 1.21$, 143 dof). Freeing both the normalization and photon indices we obtain an improved fit (nhp = 0.22, $\chi^2_r = 1.09$, 141 dof). An f test (Bevington 1969) shows that
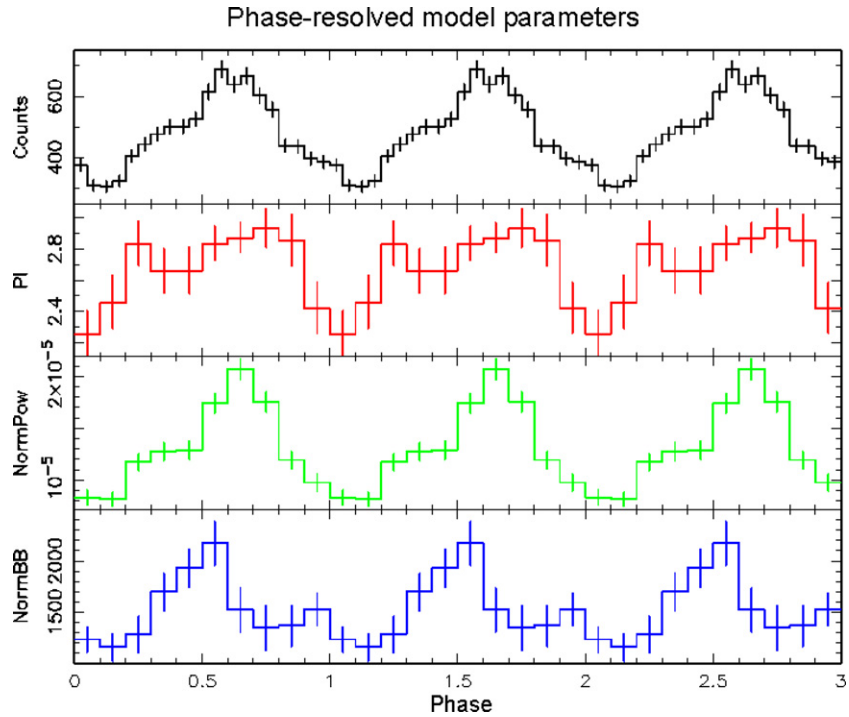
Figure 3. Best-fit phase-resolved X-ray spectral parameters of PSR J1741−2054, plotted as a function of the pulsar phase, defined as in Figure 2. As discussed in Section 7, the power law (third panel from the top) and blackbody (panel 4) normalizations and the photon index (panel 2) evolve throughout the pulsar phase.
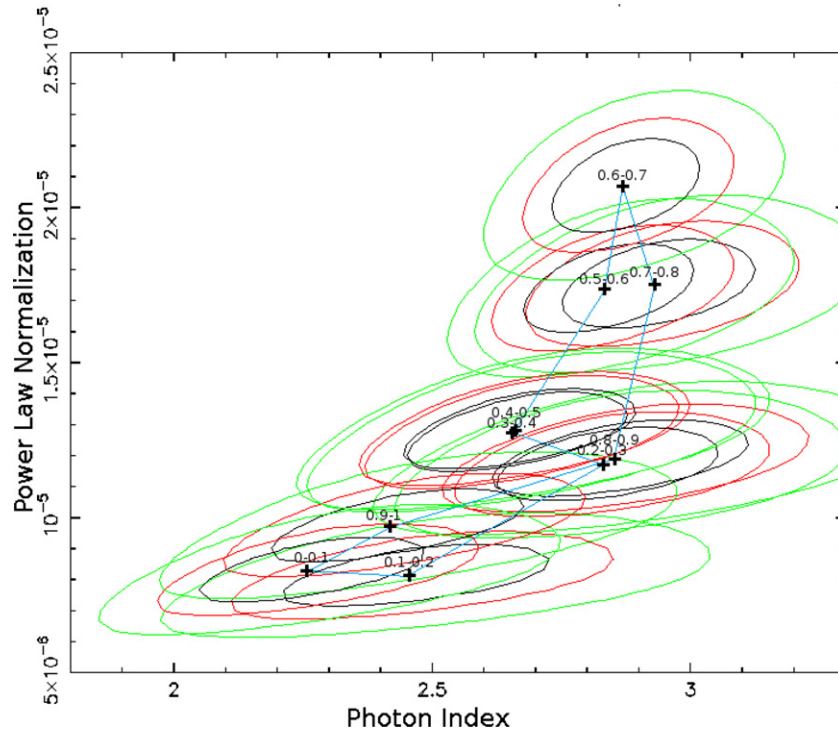

Figure 4. Confidence contours for the 10 bin X-ray phase-resolved analysis of PSR J1741−2054, showing the pulsar photon index and the power-law normalization. Black contours are at the 1σ confidence level, red at 90%, and green at 3σ. Blue lines follow the pulsar phase.

the probability for a chance improvement is 2.6×10^{-4}, pointing to a significant effect when both the power-law normalization and photon index are free to vary. Next, we fixed the power-law values obtained in the previous fit and evaluated the blackbody component in the 0.3–0.7 keV energy band. Thawing only the blackbody normalization, we obtain an nhp = 0.74 ($\chi^2_r = 0.93$, 128 dof). A variation of the blackbody temperature

with pulsar phase is not statistically compelling; however, the high pulsed fraction at low energies implies significant pulsation of the blackbody normalization.

The blackbody normalization and power-law normalization and photon index vary with pulsar phase. We divided our data set into 10 phase bins, each with width 0.1 and containing ∼1000 counts, and fitted the obtained spectra fixing the column density

and linking blackbody temperatures. We obtained the curves reported in Figure 3, with the photon index gradually increasing with phase and the normalizations following the light curve, with no statistically significant differences between blackbody and power-law peaks. The variation in photon index is also shown by the confidence contours for the 10 phase bins, plotted in Figure 4 for the plane of the index and the power law normalization. The variation with blackbody normalization is similar.

8. DISCUSSION AND CONCLUSIONS

By analyzing the new *XMM-Newton* observation of PSR J1741−2054, we fully characterized the high-energy emission of this nearby middle-age radio-faint pulsar.

Its nebular emission is typical of pulsar wind nebulae, both for its non-thermal spectrum and for the flux decrease with distance along the tail emanating from the pulsar. A hint of nebular spectral variation with distance from the pulsar is detected. The shattered shape of the nebula is peculiar and a deeper analysis of the new *Chandra* data is needed to better understand this unusual behavior. These observations could also provide a measurement of the pulsar proper motion. Such an analysis is beyond the scope of this work.

Modeling the X-ray spectrum of the pulsar requires a composite model, summing thermal and non-thermal components. Both components are ∼35%–40% pulsed, with single-peaked light curves and maxima phase-aligned to within 0.1 in phase. While the thermal light curve is compatible with a sinusoid, the non-thermal profile has a sharper peak. The best-fitting thermal spectrum yields a temperature ($\sim 7 \times 10^5$ K), compatible with the theoretical expectations for the cooling of a 390 kyr old pulsar (Pons et al. 2009). We note that the best-fit temperature of the nsa model ($\sim 3 \times 10^5$ K) is below the theoretical expectations, further disfavoring such a model. A pulsed component from thermal cooling has already been noted for several pulsars (Caraveo et al. 2004; De Luca et al. 2005; Manzali et al. 2007), and that of PSR J1057−5226 has a similar pulsed component. Such pulsations can be ascribed to a dependence of the observed emitting area on the line of sight. Halpern & Ruderman (1993) describe a magnetospheric "blanket" caused by cyclotron resonance scattering off the plasma in the magnetosphere that could screen the thermally emitting surface during specific phase intervals, depending on the magnetic field configuration and viewing geometry. Anisotropic heat transfer from the pulsar interior can also explain flux variation across the neutron star surface (Greenstein & Hartke 1983). If the thermal component is due to the cooling of the entire neutron star surface (12 km radius) from the thermal normalization in the best-fit spectrum (which depends only on the pulsar distance and the emitting radius), we can derive the pulsar distance to be ∼850 pc, with 3σ limits of ∼650 and ∼1100 pc (e.g., Halpern et al. 2007). On the other hand, thermal emission from polar caps heated due to downstreaming of $e^{\pm}$ (Harding & Muslimov 2002), as seen in the case of PSR J0007+7303 in the CTA 1 supernova remnant, is expected to be generated from much smaller regions (<100 m, based on a simple "centered" dipole magnetic field geometry, De Luca et al. 2005; Marelli et al. 2013), which would imply an unrealistic pulsar distance smaller than 10 pc. Distances lower than a few hundred parsecs are greatly disfavored due to the non-negligible value of the column density (about one fourth of the total Galactic column density in this direction). We note that a distance of 850 pc would result in a 110% γ-ray efficiency, defined as $L_\gamma/\dot{E}$, with L_γ the luminosity above 100 MeV. The distance range cited above implies an efficiency range of 60%–180%. Similarly, the X-ray efficiency would be ∼1.2% (0.7%–2.1%). Such an unrealistic γ-ray efficiency could be explained by a beaming factor f_Ω less than 1 (as defined in 2PC), or by a moment of inertia larger than 10^{45} g cm^2.

A 10 bin phase-resolved X-ray spectral analysis reveals variations in the X-ray photon index in addition to the phase-varying normalizations of the two spectral components, with a softer spectrum during the on-pulse phases (Figure 3). It is difficult to compare the behavior of J1741 with that of other *Fermi* pulsars, since the Crab is the only one for which such variation was detected, and the Crab's non-thermal spectrum becomes softer in the primary-pulse maximum and harder during the bridge between the two maxima (Weisskopf et al. 2011). Although some models have been developed to explain the Crab's optical-to-γ-ray behavior (see, e.g., Harding et al. 2008; Tang et al. 2008; Hirotani 2008), the physics behind the pulsar's X-ray photon index variations are still unclear.

Moreover, unlike the Crab, the γ-ray, X-ray, and radio peaks of PSR J1741−2054 are not aligned, pointing to a clear difference in the geometry and/or altitude above the neutron star surface of the different emitting regions. Indeed, the γ-ray and X-ray peaks are phase-offset by roughly a half rotation, as is also seen in PSRs J0007+7303, J1057−5226, and J0659+1414 (De Luca et al. 2005; Caraveo et al. 2010). Although these differences are expected from different models for the radio and γ-ray bands (Abdo et al. 2013), no model is able to account for the offset between γ-ray and X-ray peaks. The alignment between the thermal and non-thermal X-rays (seen also in other pulsars, e.g., J0659+1414 and J1057−5226), as well as the phase lag with the γ-ray emission coming from the outer magnetosphere, can suggest that the non-thermal emission is generated in a region near the pulsar poles (e.g., in a polar cap emission model). Also, the low X-ray luminosity of radio-quiet pulsars in the X-ray band (Marelli et al. 2011) suggests that the radio and X-ray emission regions may be in close proximity. The origin of the phase lag between the radio and X-ray light curves is unclear. A comprehensive study of pulsar high-energy light curves and phase-resolved spectra will be crucial to understanding the X-ray emission mechanisms and geometry.

REFERENCES

Abdo, A. A., Ackermann, M., Ajello, M., et al. 2009a, Sci, 325, 840
Abdo, A. A., Ackermann, M., Ajello, M., et al. 2009b, Sci, 325, 848
Abdo, A. A., Ajello, M., Allafort, A., et al. 2013, ApJS, 208, 17
Atwood, W. B., Abdo, A. A., Ackermann, M., et al. 2009, ApJ, 697, 1071
Becker, W. 2009, Neutron Stars and Pulsars (Astrophys. Space Sci. Lib. Vol. 357; Berlin: Springer),
Bevington, P. R. 1969, Data Reduction and Error Analysis for the Physical Sciences (New York: McGraw-Hill)
Camilo, F., Ray, P. S., Ransom, S. M., et al. 2009, ApJ, 705, 1
Caraveo, P. A. 2013, arXiv:1312.2913
Caraveo, P. A., De Luca, A., Marelli, M., et al. 2010, ApJ, 725, 6
Caraveo, P. A., De Luca, A., Mereghetti, S., Pellizzoni, A., & Bignami, G. F. 2004, Sci, 305, 376
Cheng, K. S., Ho, C., & Ruderman, M. 1986, ApJ, 300, 500
Cordes, J. M., & Lazio, T. J. W. 2002, arXiv:astro-ph/0207156
De Jager, O., & Busching, I. 2010, A&A, 517, 9
De Luca, A., Caraveo, P. A., Mereghetti, S., Negroni, M., & Bignami, G. F. 2005, ApJ, 623, 1051
Dickey, J. M., & Lockman, F. J. 1990, ARA&A, 28, 215
Espinoza, C. M., Guillemot, L., Celik, O., Weltevrede, P., & Stappers, B. W. 2013, MNRAS, 430, 571
Garmire, G. G., Bautz, M. W., Ford, P. G., et al. 2003, Proc. SPIE, 4851, 28
Greenstein, G., & Hartke, G. J. 1983, ApJ, 271, 283
Halpern, J. P., Camilo, F., & Gotthelf, E. V. 2007, ApJ, 668, 1154
Halpern, J. P., & Ruderman, M. 1993, ApJ, 415, 286
Harding, A. K. 2013, JASS, 30, 145
Harding, A. K., & Muslimov, A. G. 2002, ApJ, 568, 862
Harding, A. K., & Muslimov, A. G. 2004, Proc. 35th COSPAR Scientific Assembly, 562
Harding, A. K., Stern, J. V., Dyks, J., & Frackowiak, M. 2008, ApJ, 680, 1378
Hirotani, K. 2008, ApJ, 688, 25
Jackson, M. S., & Halpern, J. P. 2005, ApJ, 633, 1114
Kalberla, P. M., Burton, W. B., & Hartmann, D. 2005, A&A, 440, 775
Keith, M. J., Johnston, S., Ray, P. S., et al. 2011, MNRAS, 414, 1292
Kerr, M. 2011, ApJ, 732, 38
Manzali, A., De Luca, A., & Caraveo, P. A. 2007, ApJ, 669, 570
Marelli, M. 2012, arXiv:1205.1748
Marelli, M., De Luca, A., & Caraveo, P. A. 2011, ApJ, 733, 82
Marelli, M., De Luca, A., Salvetti, D., et al. 2013, ApJ, 765, 36
Mattox, J. R., Bertsch, D. L., Chiang, J., et al. 1996, ApJ, 461, 396
Nolan, P. L., Abdo, A. A., Ackermann, M., et al. 2012, ApJS, 199, 31
Pierbattista, M., Grenier, I. A., Harding, A. K., & Gonthier, P. L. 2012, A&A, 545, 42
Pierbattista, M., Harding, A. K., & Grenier, I. A. 2014, A&A, submitted (arXiv:1403.3849)
Pletsch, H. J., Guillemot, L., Allen, B., et al. 2013, ApJ, 779, 11
Pons, J. A., Miralles, J. A., & Geppert, U. 2009, A&A, 496, 207
Protassov, R., Van Dyk, D. A., Connors, A., et al. 2002, ApJ, 571, 545
Ransom, S. M., Ray, P. S., Camilo, F., et al. 2011, ApJ, 727, 16
Ray, P. S., Kerr, M., Parent, D., et al. 2011, ApJS, 194, 17
Romani, R. W., Shaw, M. S., Camilo, F., Cotter, G., & Sivakoff, G. R. 2010, ApJ, 724, 908
Saz Parkinson, P. M., Dormody, M., Ziegler, M., et al. 2010, ApJ, 725, 571
Struder, L., Briel, U., Dennerl, K., et al. 2001, A&A, 365, L18
Tang, A. P. S., Takata, J., Jia, J. J., & Cheng, K. S. 2009, ApJ, 676, 562
Turner, M. J. L., Abbey, A., Arnaud, M., et al. 2001, A&A, 365, 27
Wang, Z., Breton, R. P., Heinke, C. O., Deloye, C. J., & Zhong, J. 2013, ApJ, 765, 151
Watters, K. P., & Romani, R. W. 2011, ApJ, 727, 123
Weisskopf, M. C., Tennant, A. F., Yakovlev, D. G., et al. 2011, ApJ, 743, 139